Tunable Directional Emission and Collective Dissipation with Quantum Metasurfaces

D. Fernández-Fernández[1,2] and A. González-Tudela[1,*]
[1]Institute of Fundamental Physics IFF-CSIC, Calle Serrano 113b, 28006 Madrid, Spain
[2]Instituto de Ciencia de Materiales de Madrid ICMM-CSIC, 28049 Madrid, Spain

(Received 2 July 2021; accepted 26 January 2022; published 14 March 2022)

Subwavelength atomic arrays, recently labeled as quantum metamaterials, have emerged as an exciting platform for obtaining novel quantum optical phenomena. The strong interference effects in these systems generate subradiant excitations that propagate through the atomic array with very long lifetimes. Here, we demonstrate that one can harness these excitations to obtain tunable directional emission patterns and collective dissipative couplings when placing judiciously additional atoms nearby the atomic array. For doing that, we first characterize the optimal square array geometry to obtain directional emission patterns. Then, we characterize the best atomic positions to couple efficiently to the subradiant metasurface excitations and provide several improvement strategies based on entangled atomic clusters or bilayers. Afterward, we also show how the directionality of the emission pattern can be controlled through the relative dipole orientation between the auxiliary atoms and the one of the array. Finally, we benchmark how these directional emission patterns translate into to collective, anisotropic dissipative couplings between the auxiliary atoms by studying the lifetime modification of atomic entangled states.

DOI: 10.1103/PhysRevLett.128.113601

The modification of atomic radiation by the presence of other atoms has been a very active of area in quantum optics since the seminal work by Dicke [1]. There, he showed that an atomic ensemble confined within a volume smaller than their optical wavelength (λ_0) emits photons with a collectively enhanced decay rate [2] due to the photon-mediated interactions appearing between them [3,4]. With the advent of optical lattices [5,6], the focus expanded to atomic arrays. Few works considered first the modification of the photonic energy dispersion for arrays with interatomic distances $d \sim \lambda_0$ [7–14]. However, the interest in the field exploded by studying the properties of (deeply) subwavelength arrays, that is, when $d < (\ll)\lambda_0$ [15–38]. For such distances, interference leads to collective atomic responses very different from their individual one, like in metamaterials [39], and which can be harnessed to improve photon-storage fidelities [17] and quantum registers [29], to generate multiphoton states [34], or to obtain chiral [30] or magnetic [35] light-matter interfaces. These prospects have placed such "quantum metamaterials" [34] at the spotlight, triggering several experiments [40,41].

One of the most remarkable features of these systems is that they host subradiant excitations that propagate confined within them [17–28] with very long lifetimes. These subradiant excitations display nontrivial energy dispersions, like the photons propagating in photonic crystals [42], which can be tuned modifying the array configuration. This is why recent works [36–38] have pointed out these quantum metamaterials as a platform for exploring the physics of atoms coupled to photonic crystals [43]. Compared to nanophotonics, these systems (i) do not require complicated trapping schemes to place atoms nearby dielectrics [44–49]; (ii) energy dispersions of guided modes can be modified by optical means; and (iii) different from the guided modes in photonic crystals, these subradiant modes interact [36], which can be used to induce gates [50]. So far, these initial works [36–38] have mostly considered the emergence of band-gap-mediated, coherent interactions, however, the possibilities are much richer [51–63].

One of these exciting possibilities is the generation of anisotropic dissipative couplings between emitters when energetically tuned to van Hove singularities [59–63]. Despite its incoherent nature, such directional couplings lead to the formation of bound states in the continuum [60,61,64,65], which can be instrumental to design quantum gates [66,67]. These initial works [59–61] were based on simplified models, which neglected the coupling to free-space and polarization effects. Here, we propose a realistic quantum metasurface where these phenomena can be observed and controlled through the relative orientation and position of the impurity-array atomic dipoles. In addition, we show how the emission into the subradiant modes can be increased using entangled clusters or bilayer metasurfaces. We characterize these phenomena first with a single emitter, studying its emission, and then with many, characterizing the lifetime modification of entangled states, i.e., the signature of super- and subradiance [1].

The setup we consider in this Letter is depicted in Fig. 1(a): auxiliary atoms are placed near a square atomic array with interatomic distance d. For simplicity, we consider atomic systems with a single optical transition

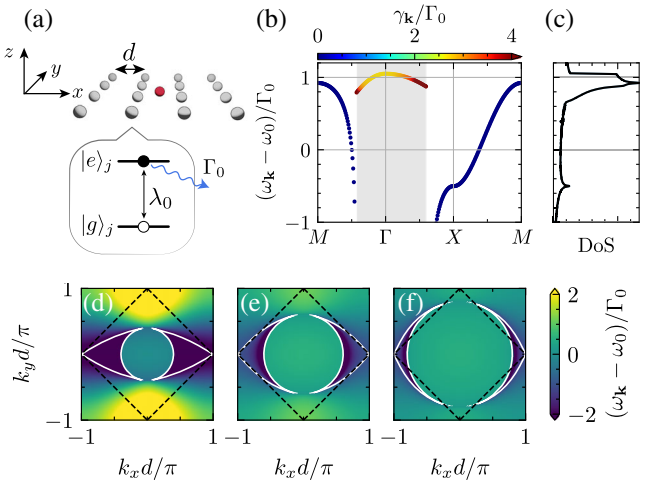

FIG. 1. (a) Impurity atoms (red) are placed near a square atomic array (gray) with lattice constant d. Each array and impurity atom has a single optical transition of wavelength $\lambda_{0/a}$ and a free-space decay rate of $\Gamma_{0/a}$. (b) Band structure for an array with in-plane polarization $\hat{\wp}_0 = \hat{\mathbf{e}}_y$ and $d/\lambda_0 = 0.3$. Color scale represents the collective decay rate, and the gray shadow region denotes the light cone. (c) Density of state in arbitrary units for the band structure shown in (b). (d)–(f) Color maps of the array band structure with (d) $d/\lambda_0 = 0.2$, (e) $d/\lambda_0 = 0.3$, and (f) $d/\lambda_0 = 0.4$. Equipotentials for the energy $\omega_{\mathbf{k}=X}$ for the metasurface (solid white) compared to the nearest-neighbor model [59–61] (dashed black).

$(e-g)$ of frequency $\omega_{a/0} = k_{a/0}c = 2\pi c/\lambda_{a/0}$ and polarization $\wp_{a/0}$ for the impurity/array atoms, respectively. Here, we focus on the situation in which the array dipoles are oriented in plane (see Supplemental Material [68] for the out-of-plane case), e.g., fixing $\wp_0 = \hat{\mathbf{e}}_y$. We leave $\wp_a$ as a free parameter, which, as we see below, will allow us to tune the emergent behavior.

Let us first characterize the properties of the metasurface. Its dynamics can be described within an stochastic wave function approach through the following non-Hermitian Hamiltonian [17]:

$$\frac{H_m}{\hbar} = \sum_{j=1}^{N}\left(\omega_0 - i\frac{\Gamma_0}{2}\right)\sigma_{ee}^{j} + \sum_{i\neq j=1}^{N}\left(J_{ij} - i\frac{\Gamma_{ij}}{2}\right)\sigma_{eg}^{i}\sigma_{ge}^{j}, \quad (1)$$

where the atom jth is located at $\mathbf{r}_j$, $\Gamma_0 = |\wp_0|^2\omega_0^3/(3\pi\hbar c^3)$ is the individual free-space decay rate, and $\sigma_{\alpha\beta}^{j} = |\alpha\rangle_j\langle\beta|$ are the dipole operators. The coherent (J_{ij}) and incoherent (Γ_{ij}) emitter interactions are given by the vacuum's Green's function [17] $\mathbf{G}_0(\mathbf{r}_i - \mathbf{r}_j)$,

$$J_{ij} - i\frac{\Gamma_{ij}}{2} = -\frac{3\pi\Gamma_0}{\omega_0}\hat{\wp}_i^* \cdot \mathbf{G}_0(\mathbf{r}_i - \mathbf{r}_j)\cdot\hat{\wp}_j, \quad (2)$$

where $\hat{\wp}_i = \wp_i/|\wp_i| \equiv \hat{\wp}_0$. In the single-excitation subspace and infinite size limit, the eigenstates of the Hamiltonian H_m are Bloch functions $S_{\mathbf{k}}^{\dagger} = (1/\sqrt{N})\sum_j \sigma_{eg}^{j} e^{i\mathbf{k}\cdot\mathbf{r}_j}$, where $\mathbf{k} = (k_x, k_y) \in [-\pi/d, \pi/d]^{\otimes 2}$, and their (complex) eigenenergies read

$$\omega_{\mathbf{k}} - i\frac{\gamma_{\mathbf{k}}}{2} = \omega_0 - \frac{3\pi\Gamma_0}{k_0}\hat{\wp}_0^* \cdot \tilde{\mathbf{G}}_0(\mathbf{k})\cdot\hat{\wp}_0, \quad (3)$$

where $\tilde{\mathbf{G}}_0(\mathbf{k}) = \sum_j e^{-i\mathbf{k}\cdot\mathbf{r}_j}\mathbf{G}_0(\mathbf{r}_j)$ is the discrete Fourier transform of the free-space tensor. In Fig. 1(b) we plot the energy dispersion $\omega_{\mathbf{k}}$ and their associated imaginary part $\gamma_{\mathbf{k}}$ (in color scale) along a path of the Brillouin zone and for an array with $d/\lambda_0 = 0.3$ [68]. As expected for such distances, interference effects lead to the sub(super)radiant character $[\gamma_{\mathbf{k}} < (>)\Gamma_0]$ of the eigenstates outside (within) the light cone. Its energy dispersion $\omega_{\mathbf{k}}$ features a saddle point at the X point, which leads to a van Hove singularity in the density of states at its energy, see Fig. 1(c). This singularity also appears in the nearest-neighbor model, and it is where the anisotropic emission and collective interactions for resonant emitters were predicted [59–61]. In that case, however, the saddle point is accompanied by straight isofrequencies, i.e., $k_x \pm (\mp)k_y = \pm\pi/d$, important for the emission directionality. The long-range nature of the photon-mediated interactions in free space [17] modify this behavior. This is shown explicitly in Figs. 1(d)–1(f), where we plot $\omega_{\mathbf{k}}$ and the corresponding isofrequency line at the X point for several d/λ_0. By doing a systematic analysis [68], we find that $d/\lambda_0 \approx 0.3$ leads to an optimal performance for in-plane polarized modes because it maximizes the isofrequency straightness, the density of states at that energy, and, as we see next, its tunability. Such subwavelength regime can be obtained by using a different optical transition for trapping the atoms than for mediating the interactions, as already done in Ref. [41]. Thus, alkaline-Earth atoms look particularly suitable since they feature optical transitions from the near ultraviolet to the infrared range [73,74].

Let us now consider the effect of placing an impurity atom near the array at position $\mathbf{r}_a$. The dynamics of the combined system is described by the Hamiltonian $H = H_a + H_{am} + H_m$, where [75]

$$\frac{H_a}{\hbar} = \left(\omega_a - i\frac{\Gamma_a}{2}\right)\sigma_{ee}^{a}, \quad (4a)$$

$$\frac{H_{am}}{\hbar} = \sum_{i=1}^{N}\left(J_{ai} - i\frac{\sqrt{\Gamma_0\Gamma_a}}{2}\right)\sigma_{eg}^{a}\sigma_{ge}^{i} + (i \leftrightarrow a). \quad (4b)$$

The impurity atom can either be the same atom or a different isotope, and if one can isolate Λ scheme in its level structure, its frequency and linewidth can be controlled with Raman-assisted transitions (see Ref. [15,38,68]). To characterize how well the impurity atoms couple to the guided modes of the metasurface, we calculate the

metasurface Purcell factor (P), that is, the ratio between the decay rate into subradiant modes (Γ_m) compared to free-space modes (Γ'). We do it using two complementary approaches. First, the semianalytical approach developed in Ref. [36],

$$P_a = \frac{\frac{9d^2}{2k_a^2}\Im\left(\iint_{|\mathbf{k}|>k_0} d^2\mathbf{k}\,\frac{\hat{\wp}_a^*\boldsymbol{\alpha}_{\mathbf{k}}(\mathbf{r}_a)\otimes\boldsymbol{\beta}_{\mathbf{k}}(\mathbf{r}_a)\hat{\wp}_a}{(\omega_a-\omega_{\mathbf{k}})/\Gamma_0}\right)}{1+\frac{9d^2}{2k_a^2}\Im\left(\iint_{|\mathbf{k}|\leq k_0} d^2\mathbf{k}\,\frac{\hat{\wp}_a^*\boldsymbol{\alpha}_{\mathbf{k}}(\mathbf{r}_a)\otimes\boldsymbol{\beta}_{\mathbf{k}}(\mathbf{r}_a)\hat{\wp}_a}{(\omega_a-\omega_{\mathbf{k}})/\Gamma_0}\right)}, \quad (5)$$

where $\boldsymbol{\alpha}_{\mathbf{k}}(\mathbf{r}_a)$ and $\boldsymbol{\beta}_{\mathbf{k}}(\mathbf{r}_a)$ are the field eigenmodes evaluated at the impurity atom position $\mathbf{r}_a$ [68],

$$\boldsymbol{\alpha}_{\mathbf{k}}(\mathbf{r}) = \sum_{j=1}^{N}\mathbf{G}_0(\mathbf{r},\mathbf{r}_j,\omega_0)\cdot\hat{\wp}_0 e^{i\mathbf{r}_j\cdot\mathbf{k}}, \quad (6a)$$

$$\boldsymbol{\beta}_{\mathbf{k}}(\mathbf{r}) = \sum_{j=1}^{N}\hat{\wp}_0^*\mathbf{G}_0(\mathbf{r}_j,\mathbf{r},\omega_0)\cdot e^{-i\mathbf{r}_j\cdot\mathbf{k}}. \quad (6b)$$

This expression is obtained under the Born-Markov approximation, which neglects retardation within the array and assumes Γ_m is much smaller than the bandwidth of $\omega_{\mathbf{k}}$. To avoid relying on this assumption and to get a better picture of real experiments, we alternatively calculate P by solving exactly the dynamics assuming an initially excited impurity atom, i.e., $\sigma_{eg}^a|\text{vac}\rangle$. Since H is excitation preserving, the system wave function at any time reads

$$|\Psi(t)\rangle = \left(C_a(t)\sigma_{eg}^a + \sum_{j=1}^{N}C_{\mathbf{r}_j}(t)\sigma_{eg}^j\right)|\text{vac}\rangle. \quad (7)$$

From this wave function, one can obtain a numerical estimation of the Purcell factor [68], which we label as P_n and which takes into account non-Markovian effects. Additionally, plotting $|C_{\mathbf{r}_j}(t)|$, one obtains the spatial emission pattern, which will be directly related to how the impurity atoms interact among them.

In Figs. 2(a) and 2(b), we plot the dependence of the Purcell factor on the vertical distance z for emitters placed above an atom or at the center of the unit cell, respectively, as well as its emission pattern (insets). We compare both the semianalytical P_a (solid lines) and the numerical approach P_n (dashed lines) for two different distances, i.e., $d/\lambda_0 =$ 0.1 and 0.3 in red and blue, respectively. Closer interatomic distances of the impurity atom to the metasurface lead to larger Purcell factors, although at the expense of losing the cross-directional emission, as expected from Figs. 1(d)–1(f). In addition, it is also at these small z regions where we see the larger deviations between the semianalytical and numerical Purcell factors. These differences can be attributed to strong deviations from the Markovian behavior [68], where P_a is not expected to work and can be attenuated by reducing Γ_a, e.g., with a Raman transition.

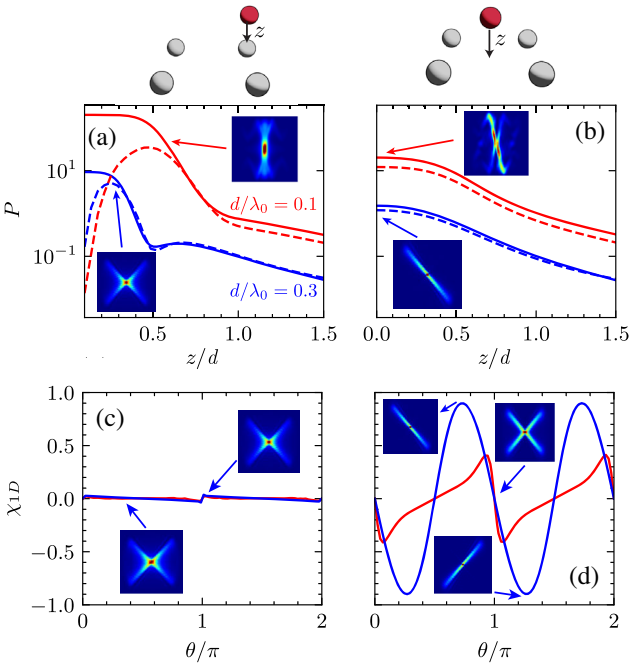

FIG. 2. (a),(b) Semianalytical (solid lines) and numerical (dashed lines) Purcell factors as function of the vertical distance of the emitter when it is located (a) on top of an atom, (b) in the center of a plaquette. The atomic array has in-plane polarization $\hat{\wp}_0 = \hat{\mathbf{e}}_y$, while the impurity atom has $\hat{\wp}_a = (\hat{\mathbf{e}}_x + \hat{\mathbf{e}}_y)/\sqrt{2}$ and a individual decay rate $\Gamma_a = 0.002\Gamma_0$. Numerical calculations have been obtained with a 50×50 dipole array. (c),(d) Directionality parameter χ_{1D} as a function of the relative orientation of the impurity-array dipoles θ, with the emitter (c) on top of a dipole at $z = 0.5d$ ($z = 0.3d$) for $\lambda_0/d = 0.1$ ($\lambda_0/d = 0.3$) and (d) in the center of a plaquette with $z = 0$. Insets show the emission patterns in real space at the points denoted by the arrows. Horizontal and vertical axes represent the x and y directions, respectively.

Apart from this deviation, another important difference of placing the impurity atom exactly above a metasurface atom [Fig. 2(a)] or at the center of the unit cell [Fig. 2(b)] is the tunability of the cross-directional emission shown in the inset of both panels. In particular, we can show that changing the relative orientation between the lattice and the impurity atom $\theta = \arccos(\hat{\wp}_0\cdot\hat{\wp}_a)$ cancels the emission along one of the directions in the former case, but not in the latter. To characterize qualitatively this tunability, we define a directional parameter [68],

$$\chi_{1D} = \sum_{|\mathbf{r}_j|\sim R}\tilde{\mathcal{P}}_j\cos[2(\theta_j-\theta_{\max})], \quad (8)$$

where $\tilde{\mathcal{P}}_j$ is the cumulative population of the dipoles located near a circle of radius R centered on the emitter, and θ_j is its angle with respect to the x axis. The maximum cumulative population is located at the angle $\theta_{\max}$. Cumulative population is renormalized so $\sum_{|\mathbf{r}_j|\sim R}\tilde{\mathcal{P}}_j = 1$. With this definition,

$\chi_{1D} = 1$ when the emission is purely one-dimensional (1D), whereas $\chi_{1D} \approx 0$ when it becomes isotropic or emits in two orthogonal directions. In Figs. 2(c) and 2(d), we plot $\chi_{1D}(\theta)$ for the impurity positions of Figs. 2(a) and 2(b), respectively, showing that $\chi_{1D}(\theta) \approx 1$ for certain θ with impurities at the center of the unit cell, whereas $\chi_{1D}(\theta) \approx 0$ at all θ for the other case.

In Fig. 2, we see how, for the most tunable situation ($d/\lambda_0 = 0.3$), the Purcell factor is limited to $P \approx 1$. Now, we explore two possible strategies to boost P while still preserving the possibility of tuning the directional emission patterns. The first strategy consists of placing pairs of emitters separated a distance d_p and prepared in a given entangled state, e.g., $|\Psi_c\rangle = (|e_{a_1} g_{a_2}\rangle \pm |g_{a_1} e_{a_2}\rangle)/\sqrt{2}$. This can be done, e.g., using dynamical optical tweezers and local spin exchange [76] or Rydberg interactions [77]. The intuition is that the interference between the atomic emission within the cluster can lead to a cancellation of free-space emission and ultimately boost P. This occurs for the antisymmetric case, obtaining $P \sim 10$, but at the price of losing the tunability of the directional emission (see Supplemental Material [68]). Since for this Letter we are interested in keeping the tunability, in Fig. 3(c) we compare the numerically obtained P_c for the symmetric cluster with the individual one P_0 for a dipole in the center of a plaquette at $z = 0$ as a function of the cluster distance d_c. Like this, one can get a moderate improvement $P_c/P_0 \approx 1.5$ for $d_c \approx 0.45d$, but keeping the directional emission. Besides, we observe an effective rotation of the emission as d_c increases, which shows that d_c can be used as a tuning knob by itself. The other strategy consists of changing the metasurface structure by a bilayer one with separation d_b, see scheme in Fig. 3(b). This structure also features straight isofrequencies [68], where one can energetically tune the impurity atom to obtain directional emission patterns. In Fig. 3(d), we numerically obtain P_b for the bilayer system and show how it can reach $P_b/P_0 \approx 7$ for either small d_b distances, keeping the 1D tunability, or for $d_b \approx 0.7$ but losing the 1D character of the emission.

After having characterized the single impurity coupling, let us consider how the directional emission patterns translate into collective dissipative interactions when more impurity atoms couple to the metasurface. One typical signature of these dissipative couplings is the lifetime renormalization of entangled atomic states [1]. This means that if an individual system decays with a rate Γ_{ind}, an entangled pair features a collective enhancement (decrease) of such decay rate $\Gamma_{\text{coll}} > (<)\Gamma_{\text{ind}}$ depending on whether it

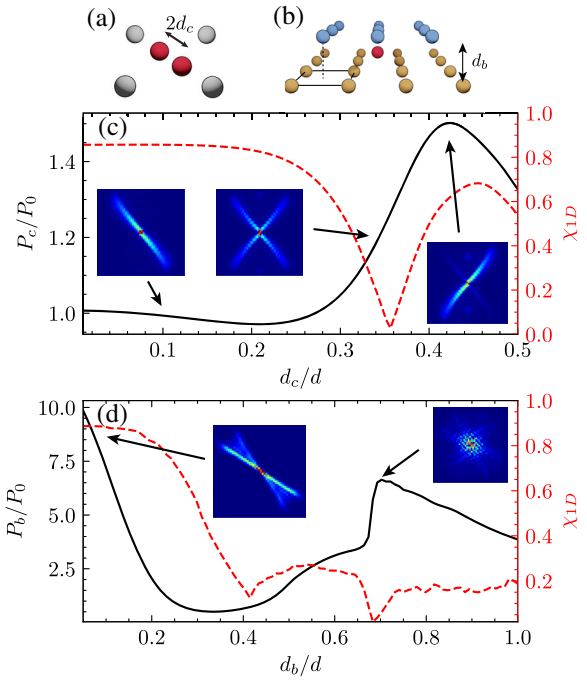

FIG. 3. (a),(b) Entangled cluster and bilayer schemes. (c),(d) Purcell factor P (solid black lines, left axis) and directionality χ_{1D} (dashed red lines, right axis) for (c) a single cluster placed near the simple metasurface and (d) a single emitter placed within a bilayer metasurface. (c) The impurities within the cluster are placed at $\mathbf{r}_{1,2} = (\pm d_c/\sqrt{2}, \mp d_c/\sqrt{2}, 0)$, with a polarization of $\hat{\wp}_a = (\hat{\mathbf{e}}_x + \hat{\mathbf{e}}_y)/\sqrt{2}$ and initialized in a symmetric state. The array has a polarization $\hat{\wp}_0 = \hat{\mathbf{e}}_y$. (d) The two layers are shifted by $(0.5d, 0.5d)$, and the emitter is located in the middle of both layers in $r_a = (0, 0.5d, d_b/2)$. The dipoles of the layers have a polarization $\hat{\wp}_0 = (\hat{\mathbf{e}}_x + \hat{\mathbf{e}}_y)/\sqrt{2}$, while for the emitter $\hat{\wp}_a = \hat{\mathbf{e}}_y$. In both cases, $d/\lambda_0 = 0.3$ and emitters are resonant with the X modes. Insets show the emission patterns in real space (x and y directions) at the configuration denoted by the arrows. Horizontal and vertical axes represent the x and y directions, respectively.

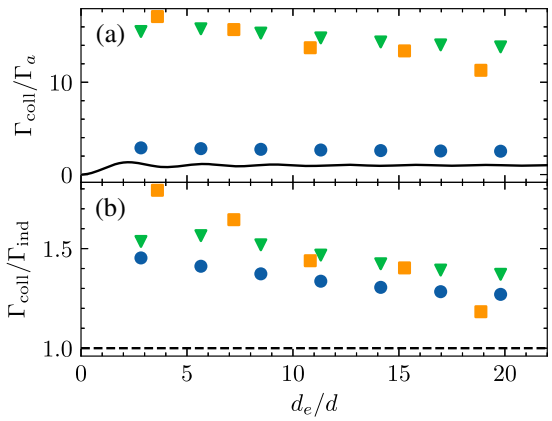

FIG. 4. (a),(b) Collective decay rates with the different strategies (a) normalized to the individual emitter decay rate in free space and (b) normalized to individual decay rate at each configuration, for a monolayer with two emitters (blue circles), a monolayer with two clusters (green triangles), and a bilayer with two emitters (orange squares). The black solid line represents the case with no metasurface. Cluster impurities distance $d_c = 0.45d$, and bilayer distance $d_b = 0.1d$. The other parameters are the same as those in Fig. 3.

is a super(sub)radiant configuration. In Fig. 4, we extract this collective enhancement Γ_{coll} as a function of the distance between impurities d_e/d through a numerical fitting of the dynamics for the three different configurations explored in Figs. 2–3: namely, (i) for a pair of impurity atoms near the single-layer array (blue dots); (ii) for a pair of entangled atomic clusters near the single-layer array (green dots); and (iii) for a pair of impurity atoms within a shifted bilayer array (orange dots). In Fig. 4(a), we plot Γ_{coll} normalized to the impurity atom free-space individual decay rate Γ_a. There we observe how, indeed, all strategies provide an improvement of collective effects compared to the case with no metasurface. To better compare the intrinsic collective dynamics induced in the different systems, in Fig. 4(b) we plot the same configurations, but normalizing Γ_{coll} to the individual decay rate Γ_{ind} in each configuration. There we observe how the bilayer enhances better collective effects at small distances due to its imperfect directionality, see Fig. 3(d), whereas the entangled cluster performs better at larger distances.

Summing up, we show how to obtain strongly directional emission patterns by placing atoms near quantum metasurfaces. We also study several strategies to achieve more efficient couplings between the impurity atoms and the directional subradiant modes of the metasurfaces based on entangled clusters or bilayer systems. Finally, we also show how these directional emission patterns translate into collective dissipative couplings when more impurity atoms couple to the metasurface. This shows the potential of quantum metasurfaces to induce nontrivial collective dissipative effects resulting from the interplay of interference and unconventional band structures. Our results can be of interest as well for subwavelength exciton arrays in 2D materials [78]. An interesting outlook is to extend this analysis to the case topological band-structure models [25,57,58].

A. G.-T. acknowledges financial support from the Proyecto Sinérgico CAM 2020 Y2020/TCS-6545 (NanoQuCo-CM), the CSIC Research Platform on Quantum Technologies PTI-001, and from Spanish project PGC2018-094792-B-100(MCIU/AEI/FEDER, EU). D. F. F. acknowledges support from the CSIC JAE Intro Research program JAEINT-20-01823/EX-0330.

Note added.—Recently, two works exploring similar ideas were published [79,80]. The code to reproduce the figures of this Letter can be found in [81].

*a.gonzalez.tudela@csic.es

[1] R. H. Dicke, Phys. Rev. **93**, 99 (1954).
[2] M. Gross and S. Haroche, Phys. Rep. **93**, 301 (1982).
[3] R. H. Lehmberg, Phys. Rev. A **2**, 883 (1970).
[4] R. H. Lehmberg, Phys. Rev. A **2**, 889 (1970).
[5] R. Grimm, M. Weidemüller, and Y. B. Ovchinnikov, in *Advances in Atomic, Molecular, and Optical Physics* (Elsevier, New York, 2000), pp. 95–170.
[6] I. Bloch, J. Dalibard, and W. Zwerger, Rev. Mod. Phys. **80**, 885 (2008).
[7] I. H. Deutsch, R. J. C. Spreeuw, S. L. Rolston, and W. D. Phillips, Phys. Rev. A **52**, 1394 (1995).
[8] D. V. van Coevorden, R. Sprik, A. Tip, and A. Lagendijk, Phys. Rev. Lett. **77**, 2412 (1996).
[9] J. A. Klugkist, M. Mostovoy, and J. Knoester, Phys. Rev. Lett. **96**, 163903 (2006).
[10] M. Antezza and Y. Castin, Phys. Rev. Lett. **103**, 123903 (2009).
[11] M. Antezza and Y. Castin, Phys. Rev. A **80**, 013816 (2009).
[12] M. Antezza and Y. Castin, Phys. Rev. A **88**, 033844 (2013).
[13] N. Bartolo and M. Antezza, Europhys. Lett. **107**, 30006 (2014).
[14] N. Bartolo and M. Antezza, Phys. Rev. A **90**, 033617 (2014).
[15] D. Porras and J. I. Cirac, Phys. Rev. A **78**, 053816 (2008).
[16] M. O. Scully, Phys. Rev. Lett. **115**, 243602 (2015).
[17] A. Asenjo-Garcia, M. Moreno-Cardoner, A. Albrecht, H. J. Kimble, and D. E. Chang, Phys. Rev. X **7**, 031024 (2017).
[18] A. Asenjo-Garcia, H. J. Kimble, and D. E. Chang, Proc. Natl. Acad. Sci. U.S.A. **116**, 25503 (2019).
[19] Y.-X. Zhang and K. Mølmer, Phys. Rev. Lett. **122**, 203605 (2019).
[20] R. J. Bettles, S. A. Gardiner, and C. S. Adams, Phys. Rev. A **94**, 043844 (2016).
[21] B. X. Wang and C. Y. Zhao, Phys. Rev. A **98**, 023808 (2018).
[22] R. J. Bettles, S. A. Gardiner, and C. S. Adams, Phys. Rev. Lett. **116**, 103602 (2016).
[23] R. J. Bettles, M. D. Lee, S. A. Gardiner, and J. Ruostekoski, Commun. Phys. **3**, 141 (2020).
[24] E. Shahmoon, D. S. Wild, M. D. Lukin, and S. F. Yelin, Phys. Rev. Lett. **118**, 113601 (2017).
[25] J. Perczel, J. Borregaard, D. E. Chang, H. Pichler, S. F. Yelin, P. Zoller, and M. D. Lukin, Phys. Rev. Lett. **119**, 023603 (2017).
[26] J. Perczel, J. Borregaard, D. E. Chang, H. Pichler, S. F. Yelin, P. Zoller, and M. D. Lukin, Phys. Rev. A **96**, 063801 (2017).
[27] R. J. Bettles, J. Minář, C. S. Adams, I. Lesanovsky, and B. Olmos, Phys. Rev. A **96**, 041603(R) (2017).
[28] D. S. Wild, E. Shahmoon, S. F. Yelin, and M. D. Lukin, Phys. Rev. Lett. **121**, 123606 (2018).
[29] A. W. Glaetzle, K. Ender, D. S. Wild, S. Choi, H. Pichler, M. D. Lukin, and P. Zoller, Phys. Rev. X **7**, 031049 (2017).
[30] A. Grankin, P. O. Guimond, D. V. Vasilyev, B. Vermersch, and P. Zoller, Phys. Rev. A **98**, 043825 (2018).
[31] P.-O. Guimond, A. Grankin, D. V. Vasilyev, B. Vermersch, and P. Zoller, Phys. Rev. Lett. **122**, 093601 (2019).
[32] A. N. Poddubny, Phys. Rev. A **101**, 043845 (2020).
[33] M. Moreno-Cardoner, D. Plankensteiner, L. Ostermann, D. E. Chang, and H. Ritsch, Phys. Rev. A **100**, 023806 (2019).
[34] R. Bekenstein, I. Pikovski, H. Pichler, E. Shahmoon, S. F. Yelin, and M. D. Lukin, Nat. Phys. **16**, 676 (2020).

[35] R. Alaee, B. Gurlek, M. Albooyeh, D. Martín-Cano, and V. Sandoghdar, Phys. Rev. Lett. **125**, 063601 (2020).
[36] S. J. Masson and A. Asenjo-Garcia, Phys. Rev. Research **2**, 043213 (2020).
[37] T. L. Patti, D. S. Wild, E. Shahmoon, M. D. Lukin, and S. F. Yelin, Phys. Rev. Lett. **126**, 223602 (2021).
[38] K. Brechtelsbauer and D. Malz, Phys. Rev. A **104**, 013701 (2021).
[39] Z. Wang, F. Cheng, T. Winsor, and Y. Liu, Nanotechnology **27**, 412001 (2016).
[40] A. Glicenstein, G. Ferioli, N. Šibalić, L. Brossard, I. Ferrier-Barbut, and A. Browaeys, Phys. Rev. Lett. **124**, 253602 (2020).
[41] J. Rui, D. Wei, A. Rubio-Abadal, S. Hollerith, J. Zeiher, D. M. Stamper-Kurn, C. Gross, and I. Bloch, Nature (London) **583**, 369 (2020).
[42] J. D. Joannopoulos, P. R. Villeneuve, and S. Fan, Nature (London) **386**, 143 (1997).
[43] D. E. Chang, J. S. Douglas, A. González-Tudela, C.-L. Hung, and H. J. Kimble, Rev. Mod. Phys. **90**, 031002 (2018).
[44] J. D. Thompson, T. G. Tiecke, N. P. de Leon, J. Feist, A. V. Akimov, M. Gullans, A. S. Zibrov, V. Vuletić, and M. D. Lukin, Science **340**, 1202 (2013).
[45] A. Goban, C.-L. Hung, S.-P. Yu, J. Hood, J. Muniz, J. Lee, M. Martin, A. McClung, K. Choi, D. Chang, O. Painter, and H. Kimble, Nat. Commun. **5**, 3808 (2014).
[46] T.-H. Chang, B. M. Fields, M. E. Kim, and C.-L. Hung, Optica **6**, 1203 (2019).
[47] A. P. Burgers, L. S. Peng, J. A. Muniz, A. C. McClung, M. J. Martin, and H. J. Kimble, Proc. Natl. Acad. Sci. U.S.A. **116**, 456 (2019).
[48] X. Luan, J.-B. Béguin, A. P. Burgers, Z. Qin, S.-P. Yu, and H. J. Kimble, Adv. Quantum Technol. **3**, 2000008 (2020).
[49] J.-B. Béguin, J. Laurat, X. Luan, A. P. Burgers, Z. Qin, and H. J. Kimble, Proc. Natl. Acad. Sci. U.S.A. **117**, 26109 (2020).
[50] C. C. Rusconi, T. Shi, and J. I. Cirac, Phys. Rev. A **104**, 033718 (2021).
[51] M. Bello, G. Platero, J. I. Cirac, and A. González-Tudela, Sci. Adv. **5**, eaaw0297 (2019).
[52] L. Leonforte, A. Carollo, and F. Ciccarello, Phys. Rev. Lett. **126**, 063601 (2021).
[53] D. De Bernardis, Z.-P. Cian, I. Carusotto, M. Hafezi, and P. Rabl, Phys. Rev. Lett. **126**, 103603 (2021).
[54] I. García-Elcano, A. González-Tudela, and J. Bravo-Abad, Phys. Rev. Lett. **125**, 163602 (2020).
[55] I. García-Elcano, J. Bravo-Abad, and A. González-Tudela, Phys. Rev. A **103**, 033511 (2021).
[56] J. Bravo-Abad, J. D. Joannopoulos, and M. Soljacic, Proc. Natl. Acad. Sci. U.S.A. **109**, 9761 (2012).
[57] A. González-Tudela and J. I. Cirac, Phys. Rev. A **97**, 043831 (2018).
[58] J. Perczel and M. D. Lukin, Phys. Rev. A **101**, 033822 (2020).
[59] F. Galve, A. Mandarino, M. G. A. Paris, C. Benedetti, and R. Zambrini, Sci. Rep. **7**, 42050 (2017).
[60] A. González-Tudela and J. I. Cirac, Phys. Rev. Lett. **119**, 143602 (2017).
[61] A. González-Tudela and J. I. Cirac, Phys. Rev. A **96**, 043811 (2017).
[62] S.-P. Yu, J. A. Muniz, C.-L. Hung, and H. J. Kimble, Proc. Natl. Acad. Sci. U.S.A. **116**, 12743 (2019).
[63] A. González-Tudela and J. I. Cirac, Quantum **2**, 97 (2018).
[64] C. W. Hsu, B. Zhen, A. D. Stone, J. D. Joannopoulos, and M. Soljačić, Nat. Rev. Mater. **1**, 16048 (2016).
[65] A. Feiguin, J. J. García-Ripoll, and A. González-Tudela, Phys. Rev. Research **2**, 023082 (2020).
[66] V. Paulisch, H. J. Kimble, and A. González-Tudela, New J. Phys. **18**, 043041 (2016).
[67] A. F. Kockum, G. Johansson, and F. Nori, Phys. Rev. Lett. **120**, 140404 (2018).
[68] See Supplementary Material at http://link.aps.org/supplemental/10.1103/PhysRevLett.128.113601 for more details on (i) how to calculate the band-structure and impurity-metasurface coupling, (ii) definition of the directionality parameter, (iii) improvement strategies, and (iv) collective dynamics of impurity atoms, which includes Refs. [69–72].
[69] S. Lorenzo, F. Lombardo, F. Ciccarello, and G. M. Palma, Sci. Rep. **7**, 42729 (2017).
[70] M. K. Agoston, *Computer Graphics and Geometric Modeling* (Springer-Verlag, Berlin, 2005).
[71] B. Olmos, D. Yu, Y. Singh, F. Schreck, K. Bongs, and I. Lesanovsky, Phys. Rev. Lett. **110**, 143602 (2013).
[72] T. Dordevic, P. Samutpraphoot, P. L. Ocola, H. Bernien, B. Grinkemeyer, I. Dimitrova, V. Vuletić, and M. D. Lukin, Science **373**, 1511 (2021).
[73] A. D. Ludlow, M. M. Boyd, J. Ye, E. Peik, and P. O. Schmidt, Rev. Mod. Phys. **87**, 637 (2015).
[74] J. P. Covey, I. S. Madjarov, A. Cooper, and M. Endres, Phys. Rev. Lett. **122**, 173201 (2019).
[75] Note, here we use the assumption commonly used in the literature that the free-space Green's function does not vary significantly for the energy ranges around ω_a, ω_0.
[76] A. M. Kaufman, B. J. Lester, M. Foss-Feig, M. L. Wall, A. M. Rey, and C. A. Regal, Nature (London) **527**, 208 (2015).
[77] T. Wilk, A. Gaëtan, C. Evellin, J. Wolters, Y. Miroshnychenko, P. Grangier, and A. Browaeys, Phys. Rev. Lett. **104**, 010502 (2010).
[78] A. Reserbat-Plantey, I. Epstein, I. Torre, A. T. Costa, P. A. D. Gonçalves, N. A. Mortensen, M. Polini, J. C. W. Song, N. M. R. Peres, and F. H. L. Koppens, ACS Photonics **8**, 85 (2021).
[79] D. Castells-Graells, D. Malz, C. C. Rusconi, and J. I. Cirac, Phys. Rev. A **104**, 063707 (2021).
[80] L. Zundel, A. Cuartero-González, S. Sanders, A. I. Fernández-Domínguez, and A. Manjavacas, ACS Photonics (2022).
[81] D. Fernandez-Fernandez, Davtax/Tunable-emission-metasurfaces: v1.0 (2022), 10.5281/zenodo.6010730.